Journal Pre-proof

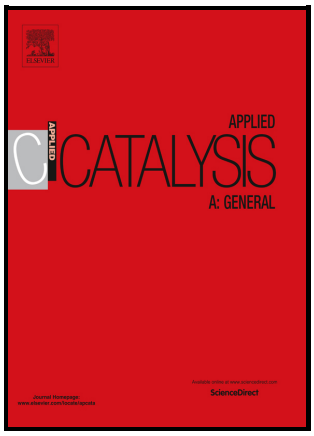

NiO/CeO_2-Sm_2O_3 nanocomposites for partial oxidation of methane: in-situ experiments by dispersive X-ray absorption spectroscopy

Lucía M. Toscani, Marina S. Bellora, Cristián Huck-Iriart, Analía L. Soldati, Joaquín Sacanell, Tereza S. Martins, Aldo Craievich, Márcia C.A. Fantini, Susana A. Larrondo, Diego G. Lamas

PII: S0926-860X(21)00371-9

DOI: https://doi.org/10.1016/j.apcata.2021.118357

Reference: APCATA118357

To appear in: *Applied Catalysis A, General*

Received date: 2 August 2021
Revised date: 2 September 2021
Accepted date: 3 September 2021

Please cite this article as: Lucía M. Toscani, Marina S. Bellora, Cristián Huck-Iriart, Analía L. Soldati, Joaquín Sacanell, Tereza S. Martins, Aldo Craievich, Márcia C.A. Fantini, Susana A. Larrondo and Diego G. Lamas, NiO/CeO_2-Sm_2O_3 nanocomposites for partial oxidation of methane: in-situ experiments by dispersive X-ray absorption spectroscopy, *Applied Catalysis A, General,* (2021) doi:https://doi.org/10.1016/j.apcata.2021.118357

NiO/CeO_2-Sm_2O_3 nanocomposites for partial oxidation of methane: in-situ experiments by dispersive X-ray absorption spectroscopy

Lucía M. Toscani[1,2,3], Marina S. Bellora [1,4], Cristián Huck-Iriart[1], Analía L. Soldati[2], Joaquín Sacanell[2,4], Tereza S. Martins[5], Aldo Craievich[6], Márcia C. A. Fantini[6], Susana A. Larrondo[3,7], and Diego G. Lamas[1,]*

[1] Instituto de Tecnologías Emergentes y Ciencias Aplicadas (ITECA), UNSAM-CONICET, Escuela de Ciencia y Tecnología, Laboratorio de Cristalografía Aplicada, San Martín, Provincia de Buenos Aires, Argentina

[2] Instituto de Nanociencia y Nanotecnología (INN), CNEA-CONICET, Argentina

[3] Instituto de Investigación e Ingeniería Ambiental, Universidad Nacional de General San Martín, San Martín, Provincia de Buenos Aires, Argentina

[4] Departamento de Física de la Materia Condensada, Gerencia de Investigación y Aplicaciones, Centro Atómico Constituyentes, Comisión Nacional de Energía Atómica, San Martín, Provincia de Buenos Aires, Argentina

[5] Departamento de Química, Instituto de Ciências Ambientais, Químicas e Farmacêuticas, Universidade Federal de São Paulo, Diadema, Brazil

[6] Departamento de Física Aplicada, Instituto de Física, Universidade de São Paulo, São Paulo, Brazil

[7] UNIDEF-CONICET-MINDEF, Departamento de Investigaciones en Sólidos, CITEDEF, Villa Martelli, Provincia de Buenos Aires, Argentina

*Corresponding author:
Diego G. Lamas
Address: ITECA, UNSAM-CONICET, Escuela de Ciencia y Tecnología, Laboratorio de Cristalografía Aplicada. Campus Miguelete, Edificio Labocluster, Av. 25 de mayo 1169, (1650) San Martín, Pcia de Buenos Aires, Argentina
Phone: +54 011 2033 1400 ext. 6072
E-mail: dlamas@unsam.edu.ar

Abstract

In this work, we analyze Sm2O3-doped CeO2 (SDC) nanopowders and NiO/SDC nanocomposites in terms of sample reducibility and catalytic activity for partial oxidation of methane. We assess the role of the average crystallite size and specific surface area in Ni and Ce reduction kinetics by in-situ X-ray absorption spectroscopy experiments in diluted H2 and CH4/O2 mixtures. Our results indicate that crystallite size and surface area play a key role in

CH4 activation through modification of the sample redox behavior. The oxidation of the metallic phase is the main cause of sample deactivation. A clear relationship is established between the temperature of maximum Ni oxidation rate and grain size. An interplay between Ce atoms from the support and Ni from the active phase was observed during the experiments, evidencing a complex relationship between oxygen vacancy concentration and catalytic activity. A high Ce3+/Ce4+ ratio in catalyst support was detrimental to catalytic activity.

Keywords: CeO_2, methane oxidation, in-situ, XANES, oxygen vacancies

Introduction

NiO/CeO_2-based composites have received great attention due to their excellent catalytic properties. The incorporation of metal oxide in the CeO_2 lattice significantly modifies the oxygen storage capacity, ionic conductivity and specific surface area of these materials, so a wide variety of materials and applications are currently under investigation. These applications include methane reforming [1-5], CO methanation [6], CO oxidation [7], oxidative dehydrogenation of propane [8], intermediate-temperature solid-oxide fuel cells anodes[9-12], etc. Particular interest is being devoted to the study of nanostructured materials, as the enhanced surface to volume ratio is expected to improve the catalytic activity [13].

CeO_2-based materials are extensively used for catalytic and electrocatalytic applications due to their redox properties [13-16]. These ceramics are widely used as supports combined with an active metallic phase because they present high specific surface area and can exchange oxygen from the lattice under reducing and oxidizing atmospheres. Oxygen vacancies created in the presence of a reducing atmosphere often act as active sites for different reactions thus improving the performance of catalysts [17]. In particular, partial oxidation of methane (POM) reaction has attracted attention, since it is a means to produce Syngas ($CO+H_2$ mixtures) and also one of the main reactions taking place in solid oxide fuel cells (SOFC) directly fueled with CH_4 [18-20]. In these applications, CeO_2 acts as a ceramic support with oxygen mobility and metallic Ni stands as the active phase for methane dehydrogenation [20].

In recent years, several members of research groups have investigated the redox behavior and catalytic properties of CeO_2-based and NiO/CeO_2-based catalysts by dispersive X-ray absorption spectroscopy (DXAS) under different atmospheres and reaction conditions [21-26]. Samples with different average crystallite sizes and specific surface areas were analyzed, finding that materials with nanometric average crystallite size and high specific surface area exhibit the best properties, achieving high reducibility and excellent methane conversion at moderate temperatures (500-800 °C). Therefore, the control of these properties is crucial for catalytic and electrocatalytic applications.

The addition of an aliovalent dopant to the CeO_2 lattice generates oxygen vacancies to

compensate charge unbalance [13]. These additional oxygen vacancies increase oxygen mobility in the material thus improving redox properties which are crucial for catalytic and electrocatalytic applications. In particular, the use of Sm_2O_3 oxide has been intensively studied as a support for several oxidation reactions and reforming reactions [27-30] and as an oxygen conducting electrolyte for SOFC applications [31].

Recent progress in the development of CeO_2-based catalysts for hydrocarbon oxidation applications has put in evidence the non-linear dependence of oxygen vacancy concentration and catalytic activity [15,29-31]. The excessive increase of surface oxygen vacancies has been reported to discourage the replenishment of active oxygen surface species and thus decreasing catalytic activity [32-34].

The addition of a metallic phase such as Ni to CeO_2-based catalysts for methane oxidation has been widely recognized to increase Ce reducibility by the presence of a strong metal-support interaction [24,34]. However, it still remains unclear if boosting Ce reducibility results in a direct increase in catalytic activity for partial oxidation of methane.

In this context, the role of sample nanostructure in the redox behavior of NiO/CeO_2-Sm_2O_3 samples is of key interest to understand CH_4 activation, particularly, in terms of the interaction between metallic and ceramic phases, the effect of the average crystallite sizes of both phases in catalytic activity and concentration of reduced species in the surface of the catalyst, namely Ce^{3+} and Ni^0.

In this work, we analyze different features of temperature programmed reduction (TPR) profiles of Ce and Ni cations in several samples under diluted hydrogen and CH_4/O_2 mixtures, namely (i) Ce reduction in Sm_2O_3-doped CeO_2 (SDC) and NiO/SDC nanopowders and (ii) Ni reduction in NiO/SDC. For this purpose, the overall reduction of the same samples was determined by conventional laboratory temperature programmed reduction in diluted H_2 and further studies were performed by in-situ synchrotron-based DXAS experiments to determine both Ce and Ni reduction degrees in both diluted H_2 and CH4/O_2 mixtures. In order to study samples with different average crystallite sizes and specific surface areas, and potentially different redox behavior, samples with different calcination temperatures were prepared, from 400 °C up to 1100°C, thus allowing to investigate and compare the reducibility and catalytic activity of several materials with different nanostructures. Particular interest is devoted to the metal-support interaction, oxygen vacancy concentration and its effect in activity toward methane oxidation.

2. Experimental procedure

2.1 Synthesis of NiO/SDC nanocomposites

NiO/SDC composites were prepared from commercial CeO_2-10 mol% Sm_2O_3 nanopowders (Nextech Materials, USA) by incipient wetness impregnation with $Ni(NO_3)_2.6H_2O$. Nickel

nitrate was dissolved in ethanol using the concentration required to obtain a nominal NiO content of 70 wt.%. After impregnation, the solids were dried at 90°C and calcined at 400°C for 2 h to convert the nickel nitrate(II) into NiO. NiO/SDC samples calcined at 650, 900 and 1100°C for 2 h were also prepared to study the influence of the average crystallite size on physicochemical properties. In the following sections, NiO/SDC samples calcined at 400, 650, 900 and 1100 °C will be labeled as NiSDC400, NiSDC650, NiSDC900 and NiSDC1100, respectively.

The NiO content of the samples was confirmed by total reflection X-ray fluorescence (TRXRF), using a Bruker S2 PICOFOX spectrometer operated with a Mo X-ray tube, with maximum power of 50W and a silicon drift detector (SDD) with an area of 10 mm^2 and resolution of 160 eV. Quantitative analysis of X-ray powder diffraction data, using the Rietveld method, also yielded similar results (see Table 1).

SDC nanopowders subjected to the same thermal treatments were also studied for the purpose of comparison. These samples will be denoted as SDC400, 650, SDC900 and SDC1100, according to their respective calcination temperatures.

2.2 Characterization techniques

Relevant features of NiO/SDC and SDC nanopowders were studied by X-ray powder diffraction (XPD), N_2-physisorption and Transmission Electron Microscopy (TEM) coupled with Energy Dispersive Spectroscopy (EDS).

XPD analyses were performed using a Bruker D8 Discover DAVINCI diffractometer operated with Cu-Kα radiation at 40 kV and 30 mA, a Ni filter and a Lynx-eye detector, in Bragg-Brentano configuration. Experimental data were collected in the angular 2θ range of 20-140° with a step size of 0.02° and a time per step of 1 s. Average crystallite sizes of the nanocrystalline phases were determined for all the samples using the Scherrer equation. Rietveld refinements were conducted by using the *Fullprof Suite* Software [35].

N_2-physisorption experiments were performed with a Quantachrome Corporation Autosorb-1 equipment. The samples were previously degassed with pure He at 90°C during 12 h. Specific surface area was evaluated using the five-point Brunauer-Emmett-Teller (BET) method [36].

Transmission electron microscopy (TEM) micrographs were obtained using a Philips CM 200 UT microscope operated at 200kV. The microscope is equipped with an ultratwin objective lens and an EDAX spectrometer for chemical analysis by Energy Dispersive Spectroscopy (EDS). Powdered samples were suspended in isopropyl alcohol, ultrasonicated for 2 minutes and deposited in Cu/ultrathin hollow carbon TEM grids (Ted Pella). The samples were dried in air at room temperature. TEM images were obtained using bright Field (BF), dark Field (DF) and high Resolution (HR) modes. Selected area electron diffraction (SAED) was used to confirm the polycrystalline phases, when possible. The average sizes of the observed (nearly isodiametric)

nanoparticles were determined from TEM images by measuring their maximum diameters with the free software ImageJ. Nanoparticle size histograms were obtained using ca. hundred individual particles and combining results from the analysis of BF, DF and HR micrographs. The average sizes determined by analyses of TEM images (D_{TEM}) are reported for all samples with their corresponding errors determined as $\sigma/(N-1)^{0.5}$, being σ the standard deviation of the size distribution. When two clearly different crystallite size modes were observed in the nanocomposites, the phases were identified by EDS and, in these cases, two separated histograms were produced (Figures S1 to S8).

2.3 Conventional laboratory temperature-programmed reduction (TPR) tests

Hydrogen TPR experiments were performed under a flow of 5 mol% H_2 in Ar (50 $cm^3(STP).min^{-1}$) for temperatures up to 800 °C with a heating rate of 10 °C.min^{-1}. These measurements were performed by using a conventional laboratory Micromeritics Chemisorb 2720 equipment. The samples were pretreated in He at 300 °C during 30 min to remove any adsorbed species on their surface. Hydrogen uptake was determined using a calibrated thermal conductivity detector (TCD).

2.4 In-situ DXAS study

X-ray absorption spectroscopy experiments in dispersive mode (DXAS) were carried out to study the evolution of the Ni^0/Ni^{2+} and Ce^{3+}/Ce^{4+} ratios with temperature and different atmosphere compositions. Experiments were performed in a temperature range of 25-800 °C in both diluted H_2 and CH_4/O_2 atmospheres.

The DXAS measurements were performed at the D06A-DXAS dispersive beamline of the UVX ring of the Brazilian Synchrotron Light Laboratory (LNLS, Campinas, Brazil). A Si (111) monochromator was used altogether with a charged coupled device (CCD) detector to collect the absorption spectrum in transmission mode. Self-supporting discs were prepared by mixing the sample powder with boron nitride that has no significant absorption in the measured energy ranges. The catalyst mass in the discs was calculated in order to obtain a total absorption ratio of 1.5. The sample discs were located in a sample-holder with a thermocouple attached to it.

The sample holder was placed in a quartz reactor, with inlet and outlet gas lines, and located in a furnace with temperature control. Inlet gas composition was set with a gas-mixing station provided with mass flow controllers and the exit composition was assessed with a Pfeiffer Omnistar mass spectrometer.

Two series of X-ray absorption near edge structure (XANES) experiments were performed in diluted H_2 (5 mol% H_2/ He balance), namely Ni K-edge and Ce L_3-edge tests. XANES spectra were collected at temperatures in the range of 400 to 800 ° C. A combination of Athena software [37] and Python scripting was used for data normalization and processing, using a

linear combination of standard spectra for analysis. NiO and metallic Ni were used as Ni^{2+} and Ni^{0} standards respectively, while $Ce(NO_3)_3.6H_2O$ and CeO_2 were used for Ce^{3+} and Ce^{4+}, respectively.

Partial oxidation of methane (POM) experiments were carried out to assess the Ni^{0}/Ni^{2+} and Ce^{3+}/Ce^{4+} ratios under catalytic operation conditions. Reactor inlet composition was of 1 $cm^3.min^{-1}$ O_2, 2 $cm^3.min^{-1}$ CH_4 and 197 $cm^3.min^{-1}$ He. Molar feed ratio was selected to be the stoichiometric ratio for POM ($CH_4:O_2 = 2$) and the spatial time was of $\tau = 0.06$ mg.min.cm^{-3}.

The samples were first heated in diluted hydrogen (5% H_2/He), with a ramp rate of 10 °C.min^{-1}, from room temperature to the maximum operating temperature of 600 °C for nanometric samples calcined at low temperatures (LT: 400°C and 650°C), and of 800 °C for samples calcined at high temperature (HT: 900°C and 1100°C). After a 20 min dwell at maximum temperature, the atmosphere was changed to the conditions detailed above for the POM reaction. The samples remained in this atmosphere for 25 min and were then cooled to 400 °C (LT samples) or 500 ° C (HT samples), following a cooling ramp rate of 10 °C.min^{-1}.

3. Results and discussion

3.1 Structural characterization

The phases present in the SDC and NiO/SDC samples, calcined at different temperatures were determined by XPD. Figure 1a and 1b display the diffractograms over the 20-80°C 2θ-range corresponding to SDC and NiO/SDC composites, respectively. This 2θ range includes the most intense Bragg peaks of both phases.

In Figure 1a the different SDC samples only exhibit the Bragg peaks corresponding to the fluorite-type crystal structure of doped ceria materials. XPD patterns shown in Figure 1b, corresponding to different NiO/SDC composites, indicate the Bragg peaks associated to the fluorite-type structure, and additional peaks, which are associated to the quasi-rock salt-type crystal structure of the NiO phase. Rhombohedral distortions are not observed in NiO diffraction patterns, in either samples calcined at low temperatures (400 °C and 650 °C), which show wide diffraction peaks, or in samples calcined at higher temperatures (900 °C and 1100 °C) that exhibit narrower peaks. Only the aforementioned phases were detected, without signs of contamination, secondary phases or evidence of reaction between NiO and SDC.

In Table 1, the average crystallite sizes of all the phases identified in the studied samples are reported, which were estimated from the width at half height of the Bragg peaks applying the Scherrer equation. As expected a priori, the average crystallite size of the SDC samples increases with increasing calcination temperature, from $D_{SDC} = 5.3$ nm for a sample calcined at 400 °C to $D_{SDC} > 100$ nm for those calcined at 1100 °C. In the case of biphasic NiO/SDC

samples, both phases exhibit the same trend observed for single-phase SDC, with the mean NiO crystallite sizes being much larger than those of the SDC phase.

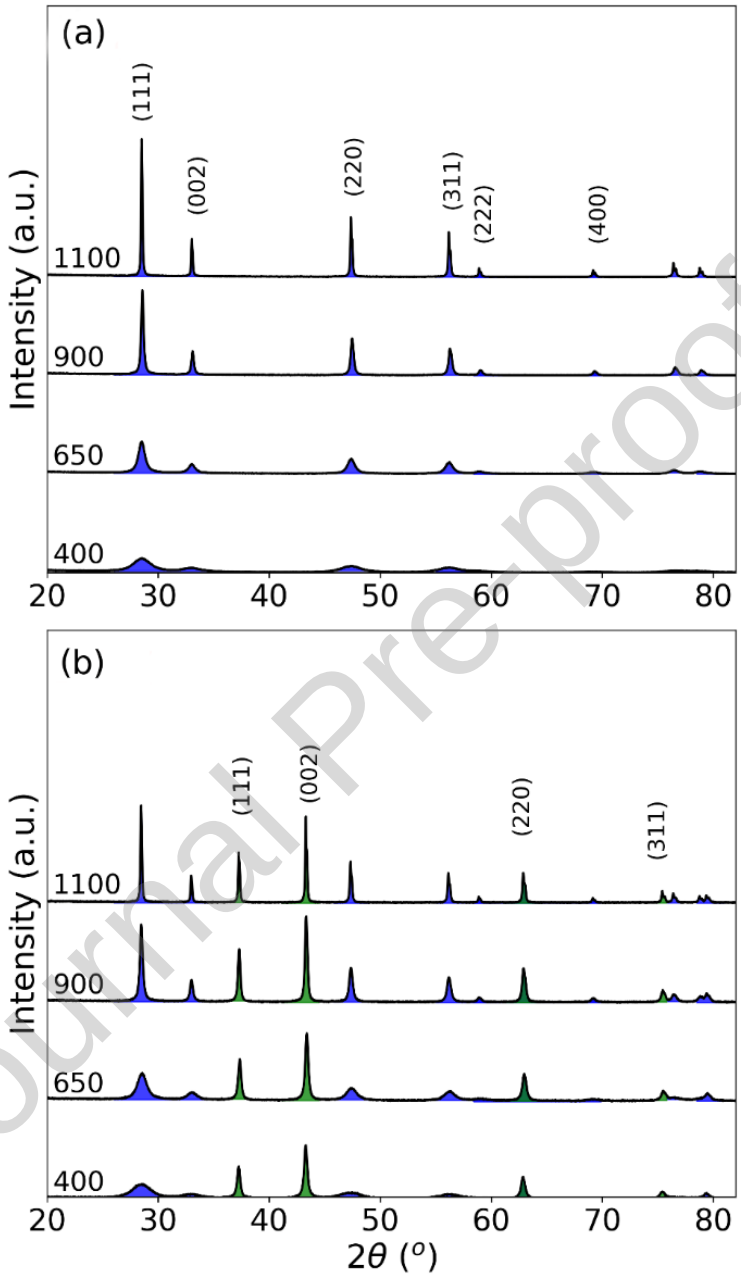

Figure 1. XPD diffractograms of fresh samples fired at the indicated temperatures, (from 400 °C up to 1100 °C): (a) single-phase SDC samples and (b) NiO/SDC two-phase nanocomposites. Bragg peaks corresponding to SDC and NiO are filled in blue and green, respectively.

Table 1. Average crystallite sizes of SDC and NiO phases (D_{SDC} and D_{NiO}, respectively) derived from XPD and TEM analyses, specific surface area (Sg), and phase content fractions (SDC and NiO mass fraction in each sample). All reported parameters excepting Sg and D_{TEM} were

determined from Rietveld refinements of the experimental XPD patterns. D_{TEM} sizes marked with (*) are equal because it was not possible to discriminate between both phases. Numbers in parentheses indicate the error in the last significant digit.

Sample	D_{SDC} (nm) XPD	D_{SDC} (nm) TEM	SDC content (wt.%) XPD	D_{NiO} (nm) XPD	D_{NiO} (nm) TEM	NiO content XPD (wt.%)	Sg ($m^2.g^{-1}$)
SDC400	5.3	4.6(1)	100	-	-	0	169
SDC650	14.6	12.1(4)	100	-	-	0	54
SDC900	55	25(1)	100	-	-	0	16
SDC1100	> 100	95(3)	100	-	-	0	5
NiSDC400	5.3	8.5(3)	31.8 (0.4)	36	42(3)	68.2 (0.5)	65
NiSDC650	9.1	8.6(4)	29.6 (0.2)	40	36(1)	70.4 (0.4)	29
NiSDC900	41	43(2)*	28.2 (0.1)	57	43(2)*	71.8 (0.4)	12
NiSDC1100	> 100	107(4)*	28.7 (0.1)	> 100	107(4)*	71.3 (0.4)	3

The Table 1 also reports another a priori expected result, namely the monotonous decrease in specific surface area in SDC samples fired at increasing temperatures, from Sg=169.5 $m^2.g^{-1}$ down to Sg=5.1 $m^2.g^{-1}$ in those fired at 1100 °C. The specific surface area is well correlated with the monotonous increase in the average crystallite size at increasing calcination temperatures. The same trend is evident for the dependence of the specific surface area with the firing temperature for NiO/SDC nanocomposites (Table 1).

The results derived from XPD analyses by applying Scherrer equation yielded the average crystallite sizes. Therefore, in order to gain an insight into the size distribution and shapes of the nanoparticles in NiO/SDC and SDC nanopowders, we have analyzed the TEM images shown in Figure 2. The average sizes determined by analyses of TEM images (D_{TEM}) are reported for all samples in Table 1.

A set of TEM images corresponding to NiO/SDC nanocomposites fired at 400, 650, 900 and 1100 °C are shown in Figures 2a, 2b, 2c and 2d, respectively. In particular, the image shown in Figure 2a referring to a sample fired at 400 °C shows two groups of particles with different morphologies which, according to EDS analysis, correspond to two different phase compositions: large squared NiO particles with D_{TEM} = 42 nm and smaller nearly spherical SDC nanoparticles with D_{TEM} = 8.5 nm. This bimodal particle size distribution is also observed for samples treated at 650°C. The TEM images of samples fired at 900°C and 1100°C show nearly polygonal nanoparticles with mean values of D_{TEM} = 43 nm and D_{TEM} = 107 nm, respectively. In these samples, it was not possible to discriminate between the two phases only by particle morphology, so we can only inform one average size.

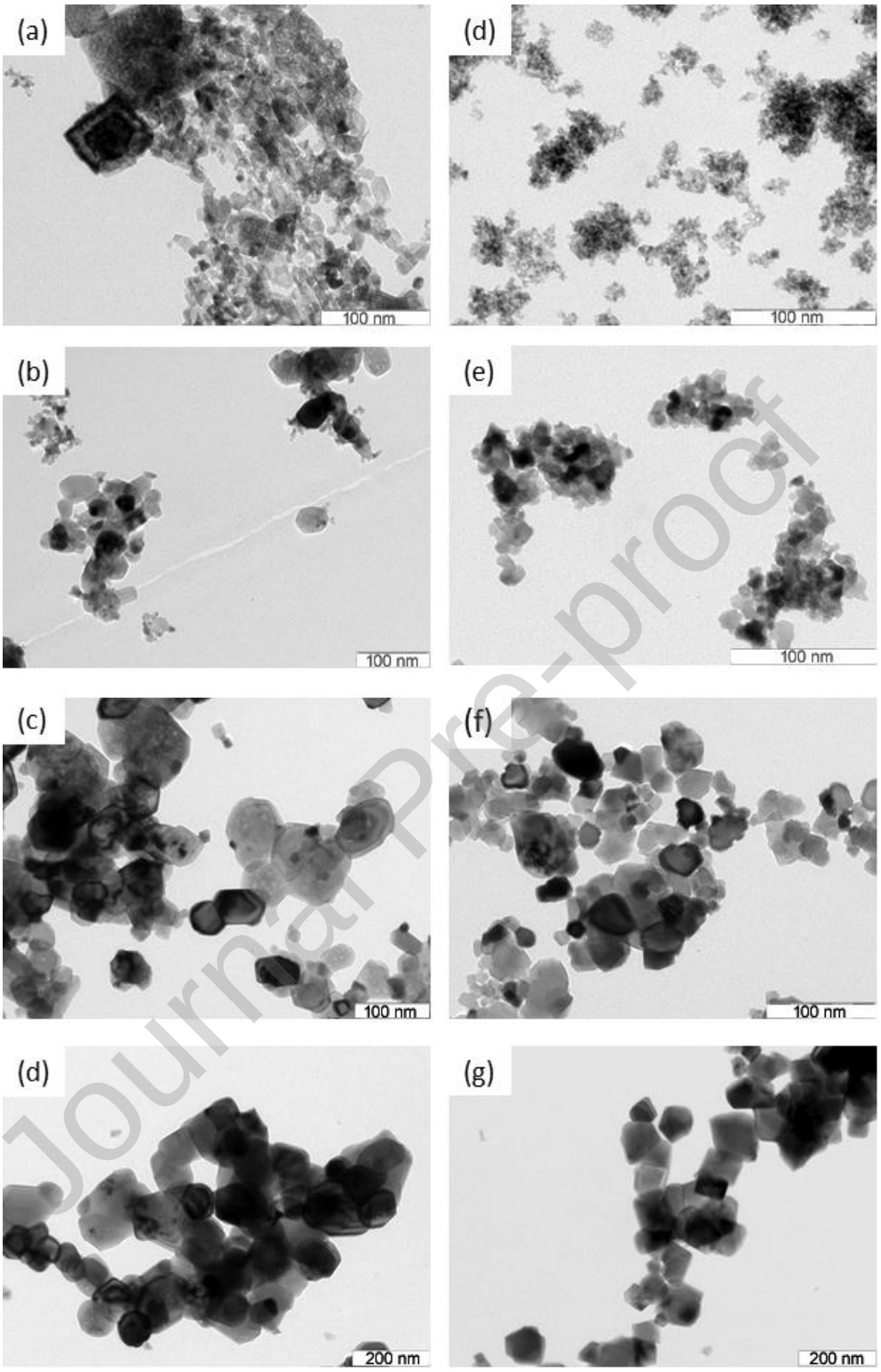

Figure 2. TEM micrographs for (a) NiSDC400 (squared particles are NiO), (b) NiSDC650 (polygonal particles are NiO), (c) NiSDC900, (d) NiOSDC1100, (e) SDC400, (f) SDC650, (g) SDC900, (h) SDC1100

A set of TEM images corresponding to SDC nanopowders fired at 400, 650, 900 and 1100 °C are shown in Figures 2e, 2f, 2g and 2h, respectively. In the sample fired at 400°C, the observed SDC nanoparticles exhibit a nearly spherical shape and are rather small (D_{TEM} = 4.6

nm). In SDC samples calcined at 650°C the average size is larger (D_{TEM} = 12.1 nm). and the particle morphology appears more irregular while in samples calcined at 900°C polygonal nanoparticles are apparent (D_{TEM} = 25 nm). In samples calcined at 1100°C the average particle size is almost four times larger.

It is worth to point out that, for all samples, BF and DF micrographs exhibited similar morphologies. Given the fact that DF images are produced by selecting a diffracted electron beam and that the sizes found in TEM and XPD analyses were similar in all cases, it can be concluded that the particles observed in BF micrographs are in fact SDC or NiO crystallites.

3.2 Reducibility of SDC and NiO/SDC samples

Figure 3a and 3b display sets of XANES spectra recorded at different temperatures corresponding to NiO/SDC sample fired at 900 °C taken at the Ce L_3- and Ni K-edges, respectively. The XANES spectra shown in Figure 3c and 3d refer to NiO/SDC sample fired at 1100 °C also recorded at the Ce L_3- and Ni K-edges, respectively (See Figures S9 and S10 with spectra of samples fired at different temperatures). In all cases, the temperature dependences of XANES spectra during the heating process indicate a clear increase in both Ce^{3+}/Ce^{4+} and Ni^0/Ni^{2+} ratios as a consequence of the reduction of Ce and Ni cations, respectively.

The experimental XANES spectra at the Ni K-edge for all studied samples were successfully fitted by using linear combinations of two (Ni and NiO) XANES standard spectra. This yielded the respective fractions of reduced Ni^0 and oxidized Ni^{2+} atoms. An example of the quality of the fitting procedures is displayed in Figure S11. In this way the relative amounts of NiO and Ni^0 were quantified for all Ni K XANES spectra and from them the temperature dependence of the degree of Ni reduction ($\varepsilon Ni = [Ni^0/(Ni^0 + Ni^{2+})]$) was calculated. The same procedure was applied to all XANES spectra acquired at the Ce L_3-edge.

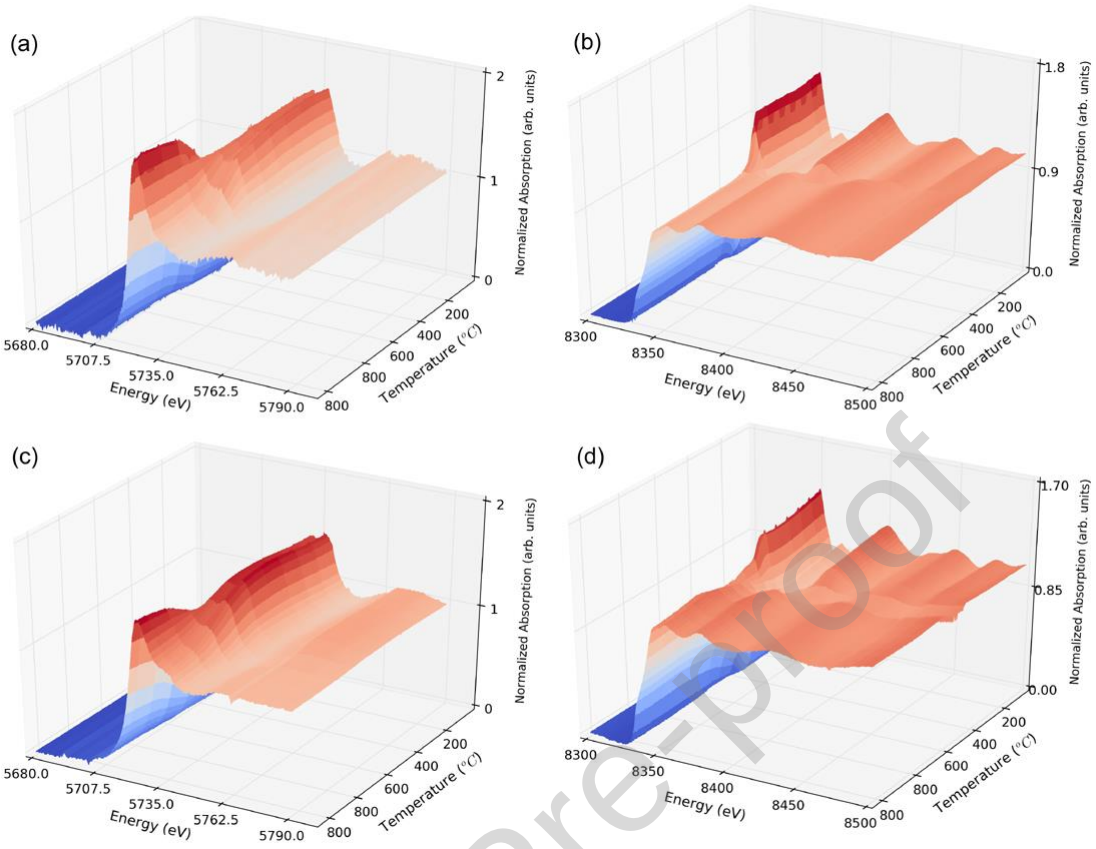

Figure 3. Selected sets of XANES spectra of NiO/SDC samples, taken at the Ce L_3- and Ni K-edges upon heating under 5 mol% H_2/He up to 800°C. (a) NiSDC900, Ce L_3-edge, (b) NiSDC900, Ni K-edge, (c) NiSDC1100 Ce L_3-edge, (d) NiSDC1100, Ni K-edge.

The temperature profiles of the degree of reduction, εCe = $[Ce^{3+}/(Ce^{4+} + Ce^{3+})]$, under reducing atmosphere were determined and are plotted in Figure 4a for different SDC samples. Notice that for samples fired at 400 °C and 650 °C the εCe values were determined from XANES spectra recorded only up to a maximum temperature Tmax=600 °C. This avoided significant crystallite growth during XANES measurements. The reduction degree of Ce (εCe) exhibits increasing trends with temperature for all SDC samples. Nonetheless, the degree of reduction of the SDC sample previously calcined at 400 °C exhibits values larger than those of samples fired at higher temperatures (650, 900 and 1100 °C) over the whole temperature range. It is worth noticing, there is no significant difference in the reduction profiles for samples fired at 900°C or 1100°C.

The reduction profiles derived from XANES analyses are consistent with the results from reduction experiments performed by using a TPR laboratory equipment displayed in Figure 5a. The reduction profiles of CeO_2-based oxides usually consist of two main peaks: a low temperature peak and a high temperature peak usually attributed to the reduction of surface and bulk species respectively [38]. In this case, it is clear that the low temperature peak decreases its

intensity with firing temperature owing to specific surface area reduction and crystallite growth. In fact, for samples SDC900 and SDC1100 this peak virtually disappears leading to a large high temperature contribution to the reduction profile consistent with reduction of bulk ceria. In these samples fired at high temperatures there is no significant difference in the Ce reduction behavior observed both by in-situ and ex-situ techniques.

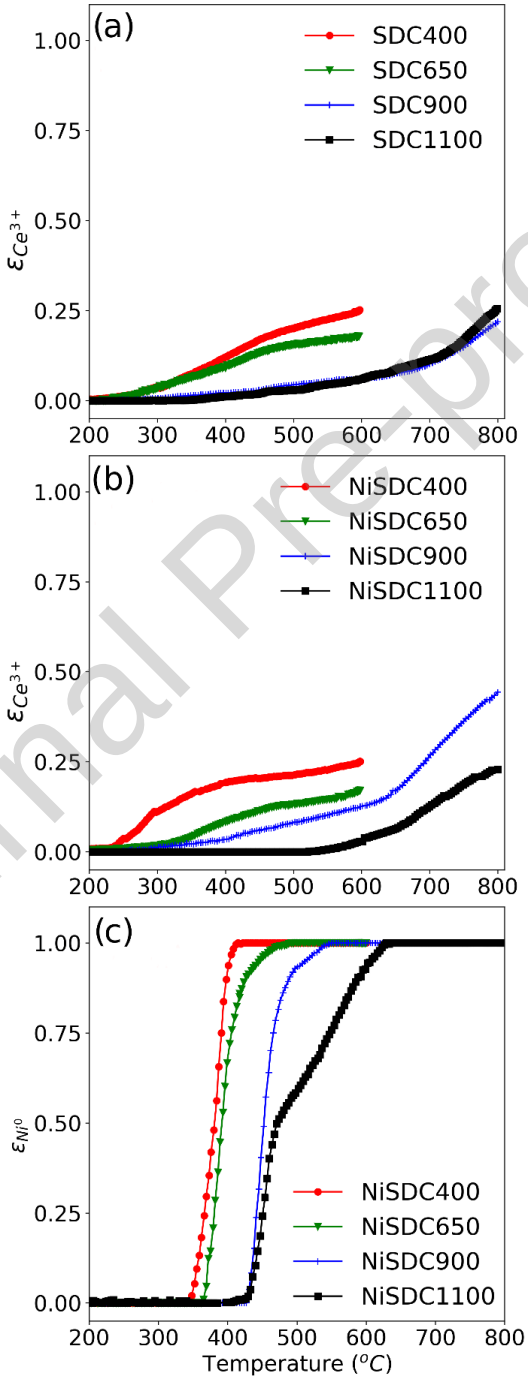

Figure 4. Degrees of Ce and Ni reduction (εCe and εNi) derived from XANES spectra recorded for (a) SDC samples at the Ce L_3-edge, (b) NiO/SDC nanocomposites at the Ce L_3-edge, (c)

NiO/SDC nanocomposites at the Ni K-edge. The displayed curves refer to four samples fired at the indicated temperatures, ranging from 400 up to 1100 °C.

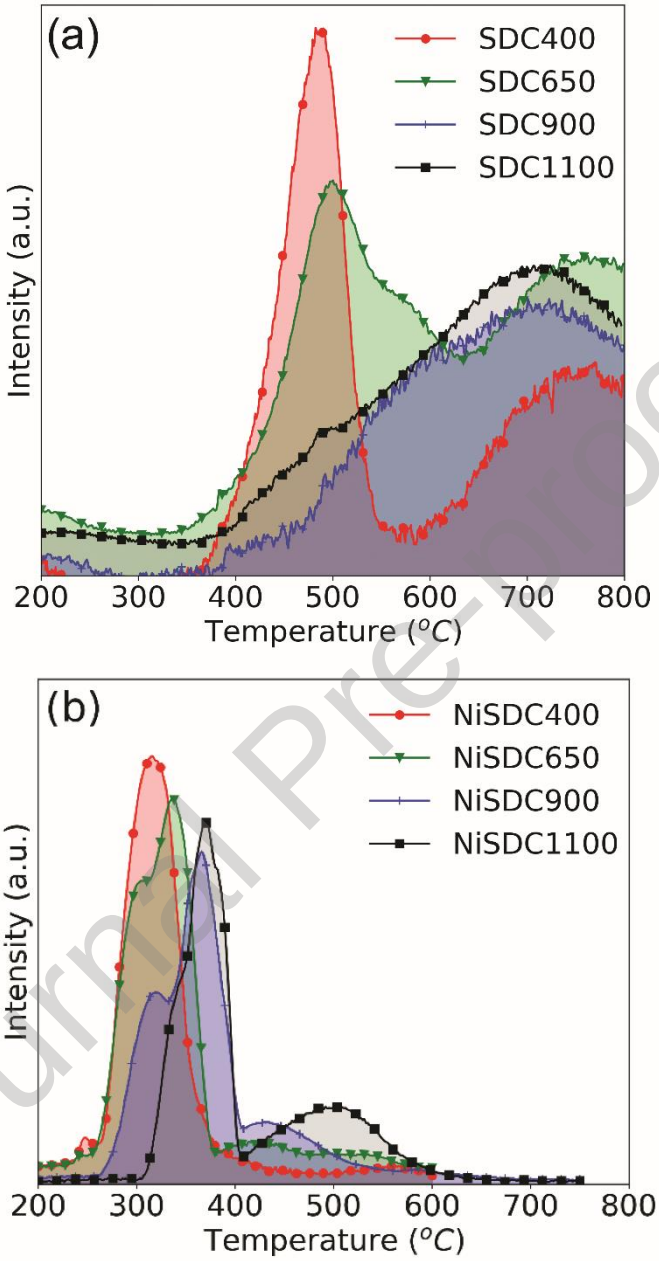

Figure 5. TPR profiles determined by using a conventional TCD detector for (a) SDC samples and (b) NiO/SDC nanocomposites. The firing temperatures of the different samples are indicated.

The temperature profiles of degree of Ce reduction (εCe) in NiO/SDC cermets plotted in Figure 4b indicate clear differences in both the Ce reduction light-off temperature and the degree of Ce reduction. The results exhibit a significant improvement in reduction kinetics for samples calcined at lower temperatures. It is noteworthy that for sample NiSDC900 (Figure 4b)

Ce reduction is enhanced when NiO is added to the system thus indicating a strong interaction of the Ce from the support with the Ni from the active phase.

Supported NiO reduction profiles usually exhibit two or more relevant features, namely low temperature contributions mostly assigned to reduction of NiO superficial free species, and a high temperature contribution generally attributed to the reduction of NiO species that strongly interact with the support [39-40]. Results from Ni reduction kinetics derived from XANES analyses are plotted in Figure 4c. It is noticeable that Ni reduction kinetics is enhanced for samples with smaller NiO average crystallites and higher specific surface area values. In particular, NiSDC400 sample exhibits a one-step NiO to Ni^0 reduction evidenced by a steep reduction growth. This is also evident from the results of TPR laboratory tests shown in Figure 5b in which a single peak is observed in the reduction profile. In the case of the results referring to NiSDC650 sample, a predominantly single step reduction profile is apparent, however, there is a change in the slope of the curve for reduction values higher than 80% (Figure 4c). This feature is clearly seen as a broad shoulder in the TPR profile between 400-500°C shown in Figure 5b. In Figure 4c it is clear that this feature becomes increasingly relevant for the NiSDC900 sample, and for NiSDC1100 it is evident as an abrupt change in the slope of the Ni reduction profile at T=450°C, correlated with a broad peak in the TPR profile plotted in Figure 5a. The wider distribution of NiO particle sizes in NiSDC1100 sample (Figure S10) can explain the change in the slope in the reduction profiles shown in Figure 4c and the broad shoulder in the TPR profile plotted in Figure 5b.

3.3 Partial oxidation of methane experiments

In this section we describe the results of in-situ POM experiments that were performed in order to gain further insight into the role of crystallite size and specific surface area on the interaction between the active phase and the support, and consequently in the catalytic activity of the studied samples. This interaction was studied by simultaneously following the oxidation state of both Ce and Ni during the catalytic experiments. As previously detailed in the experimental section, all samples were pre-reduced in diluted hydrogen and heated up to 600°C (NiSDC400 and NiSDC650) or 800°C (NiSDC900 and NiSDC1100) in this atmosphere before switching to CH_4/O_2 atmosphere.

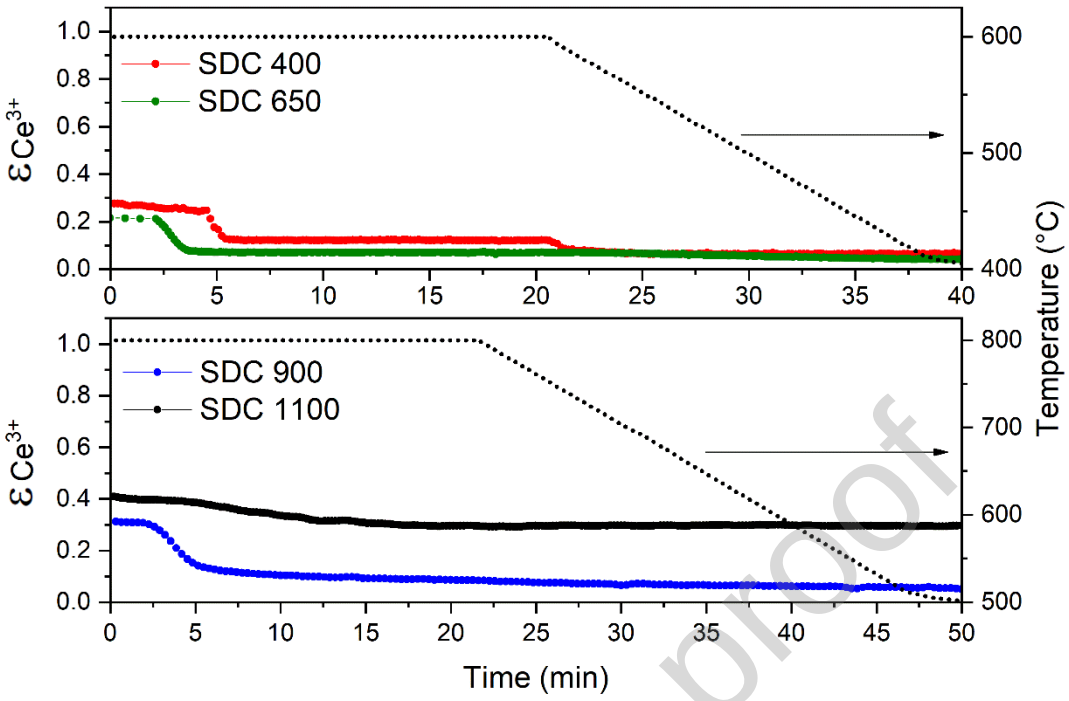

Figure 6. Time evolution of Ce^{3+} fractions (εCe) during catalytic experiments derived from XANES data for different SDC samples

Figure 6 displays the evolution of the Ce^{3+} fraction with time derived from the results of in-situ XANES experiments referring to SDC samples fired at different temperatures. SDC400 and SDC650 samples exhibit Ce re-oxidation during the first five minutes of the experiment in CH_4/O_2 atmosphere at a constant temperature of 600°C. However, re-oxidation is faster for the sample fired at 650 °C and reaches a value of Ce^{3+} fraction lower than for the sample fired at 400°C. In line with this, SDC900 and SDC1100 samples also exhibit Ce re-oxidation at the beginning of the experiment. Nevertheless, the profile referring to the SDC900 sample presents a very pronounced re-oxidation profile compared to the small and slow-changing oxidation step shown for SDC1100 sample. In addition, Ce in this last sample remains much more reduced compared to sample SDC900 achieving a value of εCe =0.29 vs εCe=0.06 at 500 °C.

Figure 7 displays the time evolution of both Ce and Ni fractions during the partial oxidation experiments for NiSDC samples fired at different temperatures. NiSDC400, NiSDC650 and NiSDC900 samples exhibit a stable Ce and Ni oxidation state while temperature is kept constant. On the other hand, NiDC1100 sample displays a slight re-oxidation of both Ce and Ni at the beginning of the experiment. After a 25 min dwell, the temperature was reduced at a rate of 10 °C.min^{-1}. It can be seen that, upon cooling in reaction conditions, all samples exhibit Ni re-oxidation.

Our results indicate that the samples fired at low temperatures (NiSDC400 and NiSDC650) exhibit a common behavior: upon cooling, at a given temperature, Ni begins to re-oxidize

displaying a steep oxidation step. This stepwise oxidation is also spotted in Ce fraction (εCe) profiles. In both cases, Ni oxidation takes place first, triggering the subsequent Ce oxidation. However, there are two clear differences between them: in the first case, maximum Ni re-oxidation takes place at T=437°C whereas in the second case it does at T = 473°C. Furthermore, the re-oxidation step is steeper in the case of NiSDC400 sample compared to NiSDC650 sample. This indicates that sample fired at 400°C remains reduced in a wider temperature range and the oxidation kinetics is faster than that of sample fired at 650°C.

Ni re-oxidation rates calculated for all samples from the slope of εNi curves are: NiSDC400: 33.6 %.°C^{-1}; NiSDC650: 24 %.°C^{-1}; NiSDC900: 23.6 %.°C^{-1}; NiSDC1100: 5.7 %.°C^{-1}. (See Figure S12). This shows that samples fired at high temperatures (NiSDC900 and NiSDC1100) exhibit the same trend: the larger the surface area the wider the temperature range in which the sample remains reduced (800-542°C for sample NiSDC900 and 800-748°C for sample NiSDC1100). The temperatures of maximum Ni re-oxidation rate are 534 °C and 671 °C for samples NiSDC900 and NiSDC1100 respectively. It is noteworthy that SDC1100 sample has a markedly broader Ni oxidation profile compared to NiSDC900 sample, indicating that re-oxidation in larger Ni grains is limited by O diffusion in the bulk.

Mass spectrometry (MS) results from catalytic experiments are exhibited in Figure 7 for all NiSDC samples (See Figure S13 and Figure S14 for MS results of SDC samples). In the first set of samples fired at low temperature, a stable reactant and product distribution is achieved a couple of minutes after the reaction conditions were established. In both cases (NiSDC400 and NiSDC650) there is H_2O, CO_2, CO and H_2 production and low O_2 values in the exhaust. However, the signals that correspond to products are not very intense compared to the other set of samples because temperature was fixed at 600°C, value at which both total and partial oxidation of methane reactions are not expected to exhibit a high yield. Finally, with the reduction of the reactor temperature, CH_4 and O_2 signals become more apparent and other signals of oxidation products begin to decrease. In samples fired at 400 °C and 650 °C, this behavior is attributed, first, to thermal deactivation and then enhanced because of Ni particle oxidation. This is evidenced with the change in the slope of product signals after Ni oxidation takes place.

Regarding the samples fired at high temperature, NiSDC1100 sample exhibits high activity towards methane oxidation, exhibiting very intense signals corresponding to CO, H_2, H_2O and CO_2. It is noteworthy that this sample remains active during dwell at 800°C and even upon cooling up to 675°C with virtually no presence of O_2 in the reactor exhaust. On the contrary, NiSDC900 sample exhibits intense CH_4 and O_2 signals during the whole experiment indicating a lower activity towards methane oxidation. In fact, the signals corresponding to methane

oxidation products exhibit a significant decrease during dwell at 800°C, a tendency that is further pronounced upon cooling in operating conditions. These results can be explained if we consider the role of oxygen vacancy concentration in catalytic activity. NiSDC900 sample exhibits a Ce^{3+}/Ce^{4+} ratio higher than 0.57 in contrast to sample NiSDC1100 that displays a stable Ce^{3+}/Ce^{4+} at around 0.35. Therefore, as Ni^{0}/Ni^{2+} is virtually stable close to unity in both cases, evidence supports that an optimum Ce^{3+}/Ce^{4+} ratio is required to modulate catalytic activity.

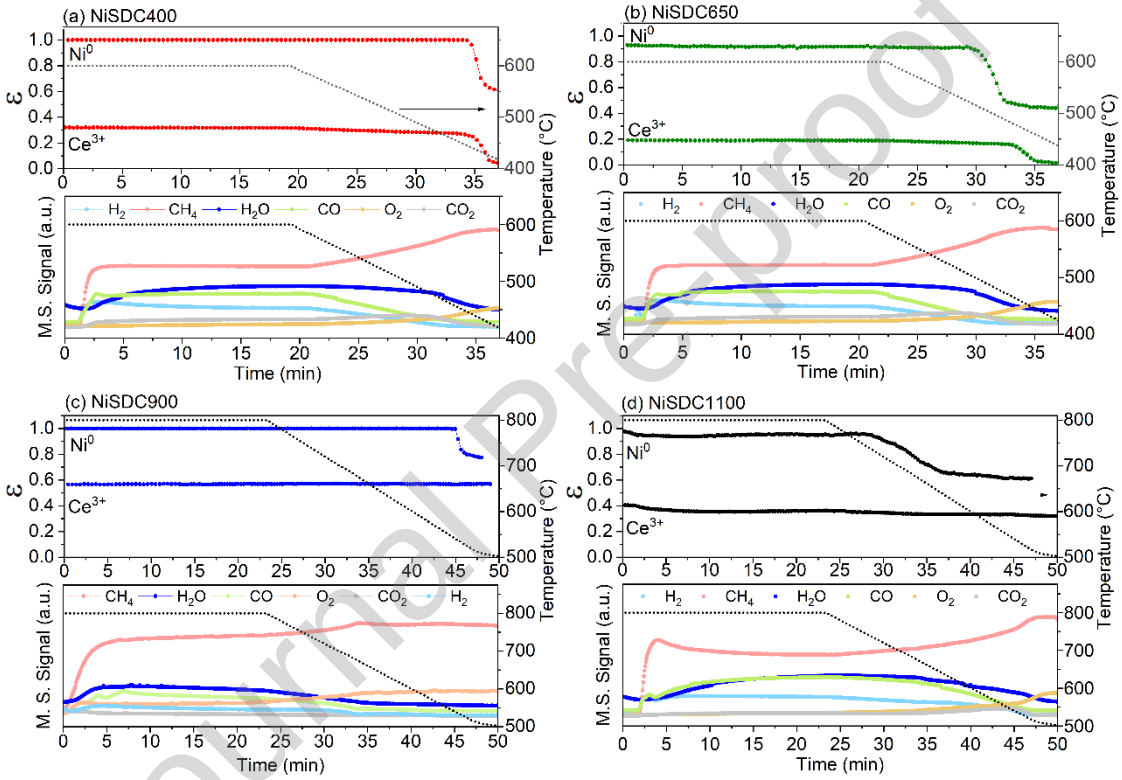

Figure 7. Mass spectrometry results from the reactor exhaust during in-situ POM catalytic experiments plotted altogether with Ni^{0} and Ce^{3+} fractions (εNi and εCe) for samples (a) NiSDC400, (b) NiSDC650, (c) NiSDC900, (d) NiSDC1100.

5. Discussion

The main aim of this work was to shed light on the relationship of relevant nanostructural features (average crystallite size and specific surface area), redox behavior and catalytic activity in NiO/CeO_2-Sm_2O_3 nanocomposites. To achieve this purpose, we have conducted two different types of in-situ experimental procedures, namely measurements of 1) temperature programmed Ce and Ni reduction under diluted H_2 and 2) catalytic experiments in CH_4/O_2 atmosphere at different temperatures. In addition, we have investigated observed correlations between these

results and the relevant structural features (crystallite size and specific surface area) of the fresh samples.

The temperature programmed reduction experiments revealed a clear relationship between Ce reduction and calcination temperature, which indicates that smaller crystallite sizes and larger surface areas enhance significantly the kinetics of the reduction reaction, especially, for samples calcined at low temperatures (400°C and 650°C). On the other hand, the samples fired at high temperatures (900°C and 1100°C) exhibited virtually the same redox behavior in diluted hydrogen.

The addition of NiO on the surface of SDC significantly affected both Ni and Ce reduction profiles revealing an enhancement in the SDC capacity to supply oxygen from the lattice at lower temperatures in contrast to the bare support. This enhancement was apparent in all cases but especially for NiSDC900 sample indicating that the high firing temperature allowed for a stronger interaction between the Ce atoms from the support and the Ni atoms from the metallic phase. This interplay was noticed in all cases by the change in slope of the Ce reduction profile when Ni is fully reduced. This evidence supports one of the mechanisms proposed for Ce reduction in materials consisting of Ce-based supports mixed with noble and transition metals as active phases, in particular Ni/CeO_2-based systems. The proposed mechanism for Ce reduction consists of the adsorptive dissociation of hydrogen on the surface of the already reduced metallic Ni particles, followed by hydrogen spillover from Ni to the oxide support [43]. This effect enables Ce reduction at lower temperatures predominantly on samples that exhibit high size dispersion of metallic Ni particles. This might explain why Ce reduction enhancement occurs in the sample NiSDC900 and not in the sample NiSDC1100. As reported in Table 1, this last sample exhibits a very low specific surface area and a high NiO average crystallite size. Moreover, clear differences were spotted in Ni reduction profiles, displaying a transition from a single abrupt step reduction toward a multi-step reduction with increasing NiO particle sizes and a wider particle size distribution. These results agree with previous findings related to bimetallic composites for which NiO reduction profiles were different for samples with different particle sizes [24]. However, our work confirms that calcination of NiO/SDC composites up to temperature up to 900 °C fully reduces NiO in a single reduction step at $T<550$°C, while for sample fired at 1100 °C full reduction occurs at $T>600$°C yielding a multi-step reduction profile.

The temperature programmed experiments presented in this work provided information on the oxygen mobility of the samples, which plays a key role on the activation of the CH_4 molecule. Huang et. al reported a clear dependence in the CO production rate during CH_4 oxidation reactions with oxygen mobility and bulk concentration [44]. This statement agrees with previous findings indicating that, once CH_4 molecule is dissociated, the oxygen atoms from the lattice are the ones involved in the oxidation of the fuel [22,44]. Considering this, since in our

work O_2 was continuously supplied in the feed flow, a sufficient oxygen concentration in the bulk was guaranteed. Thus, oxygen mobility and fast oxygen replenishment stand as the key factors limiting an efficient oxidation of CH_4.

Our results from samples fired at high temperatures (NiSDC900 and NiSDC1100) indicate that higher oxygen vacancy concentrations are detrimental for catalytic activity toward methane oxidation. A strong metal support interaction was evidenced in sample NiSDC900 that significantly modified the redox behavior of the sample, increasing drastically the Ce^{3+}/Ce^{4+} content in the sample, thus preventing an efficient catalytic behavior.

The presence of oxygen vacancies has been widely associated to a higher catalytic activity in CeO_2-based materials. This has been attributed to the highly reactive oxygen in the surface related to the oxygen vacancies [17,32]. Oxygen vacancies are created during Ce^{4+} to Ce^{3+} reduction as a mechanism for charge compensation in the oxide lattice. Thus, the larger the fraction of reduced cerium, the larger the amount of oxygen vacancies present in the lattice. Nonetheless, recent findings indicate that a moderate concentration of oxygen vacancies is required to boost catalytic activity. An excessive amount of oxygen vacancies can affect negatively oxygen mobility and, particularly affect the formation/regeneration of reactive oxygen species formed during the adsorption of O_2 from the gas phase ($O_2 \rightarrow O_2^- \rightarrow 2O^- \rightarrow 2O^{2-}$) [34]. These active oxygen species such as O_2^- or O^- deactivate through reaction with oxygen vacancies [33]. Therefore, less active surface capping oxygen (O^{2-}) is responsible for the decreased activity in samples with high vacancy concentration.

The results from the present work established the key role played by oxygen atoms from the Ce support on the activity for methane oxidation, particularly when samples exhibit different average crystallite size and specific surface area that result in a significantly different redox behavior. In NiSDC samples fired at high temperatures, the fraction of reduced ceria remained virtually constant during the whole experiment, especially in the case of the sample fired at 1100°C. This can be explained by the low specific surface area of the support that decreases its redox capacity, as also noticed in laboratory H_2-TPR experiments. Nonetheless, there seems to be an optimum Ce^{3+} fraction that enhances catalytic activity. Therefore, an increase of that fraction above the optimum value becomes detrimental to catalytic activity.

In samples fired at low temperatures the fraction of reduced ceria remains constant even during Ni oxidation, thus indicating a fast redox exchange and a surface oxygen replenishment while the catalyst is still active with a ratio of Ce^{3+}/Ce^{4+} that did not exceed 0.32 in any case. It is important to point out that immediately after Ni re-oxidation ends, Ce oxidation is triggered. These results highlight the relevance of H_2 spillover over metallic Ni in the reduction of the support in NiO/SDC nanocomposites. In line with this, another interesting result is the markedly different behavior of the SDC support in absence of Ni phase compared to that of SDC support

in NiSDC samples. In the first case, Ce re-oxidation occurs faster in the CH_4/O_2 atmosphere, whereas, in the second case, the fraction of Ce^{3+} in impregnated samples remains invariant while temperature is kept constant. This suggests that there is a clear interplay between Ce atoms from the support and Ni atoms from the active phase thus tuning the redox capacity of the sample.

It is worth noting that the variation in the specific surface area and average crystallite in both NiSDC400 and NiSDC650 samples determines the temperature at which the Ni phase becomes oxidized. Our results indicate that the larger the Ni crystallite size the slower the oxidation kinetics, thus indicating that re-oxidation is limited by oxygen diffusion in the bulk. Furthermore, the higher the specific surface area, the wider the temperature range over which sample remains active. It also worth pointing out that catalyst oxidation is one of the main causes of deactivation in Ni-based catalysts because metallic Ni sites stand as the active phase for methane decomposition [45]. Therefore, during our experiments, we have identified the temperature below which samples begin to deactivate due to re-oxidation of the active phase. In particular, as shown in Figure 8, Ni oxidation temperature decreases with increasing specific surface area. In addition, taking into consideration that specific surface area, Sg, is inversely proportional to the average grain size, D_{BET}, a clear relationship between sample grain size and activity towards fuel oxidation was established. In this case, an increase in grain size triggers Ni re-oxidation of the sample at a higher temperature. This was evidenced in the change in the slope of the signals corresponding to oxidation product in the reactor exhaust upon cooling in all samples except for sample NiSDC900. This sample presented signs of deactivation from the beginning of the experiment because of the elevated Ce^{3+}/Ce^{4+} content in the support.

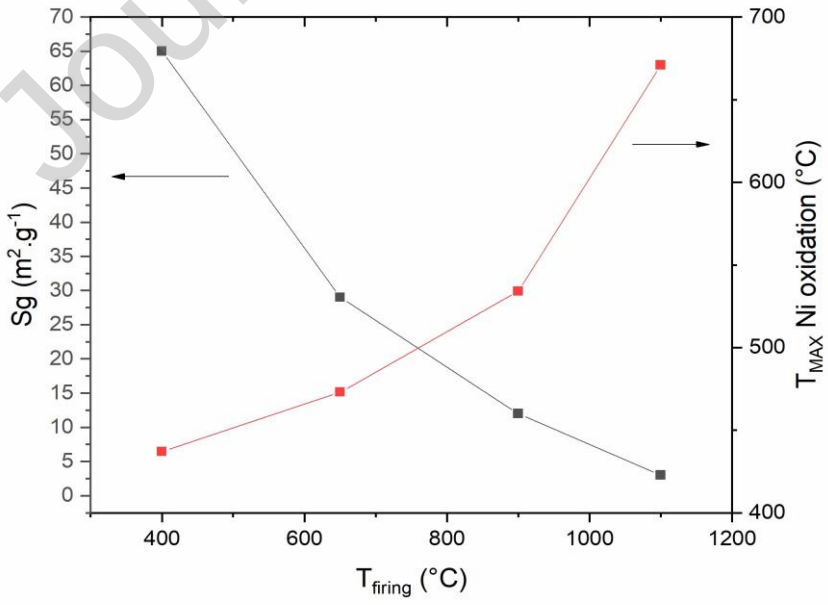

Figure 8. Temperature dependence of the specific surface area of samples (black symbols) and temperatures at which maximum oxidation rate occurs (red symbols).

6. Conclusions

We have studied by in-situ XANES spectroscopy the relationship between catalytic activity and relevant structural features - such as average crystallite size and specific surface area - of NiO/CeO_2-Sm_2O_3 nanocomposites.

Our experimental results demonstrate that the redox behavior of the studied samples depends significantly on their average crystallite size and specific surface area. SDC samples fired at different temperatures exhibit different reduction kinetics, particularly in the case of those fired at low temperatures, which exhibit decreasing light-off temperatures for smaller crystallite sizes. The addition of a NiO phase to the SDC support enhances oxygen supply from the lattice and reinforces the influence of grain size in the Ce reduction profile. NiO reduction profiles in Ni/SDC samples exhibit a transition from a single step reduction to multi-step reduction profiles for increasing NiO particle sizes and wider particle size distributions. Not only the reduction kinetics is modified but also a shift toward low temperature was observed for samples with smaller crystallite sizes, achieving in all cases a full phase reduction at $T < 600°C$.

During the course of the experiments in diluted H_2 and in CH_4/O_2 atmospheres, a clear interplay between SDC and NiO phases was observed. When Ni is added to the system, a shift in the reduction temperature is observed. Moreover, when full Ni reduction is achieved, a change in the slope of Ce reduction profile is apparent. This provides a strong evidence of the presence of H_2 spillover in the metallic phase that enhances Ce reduction. This enhancement in Ce reduction is further accelerated when complete Ni reduction is achieved. This behavior was visible in all cases but especially for NiSDC900 sample, indicating that higher firing temperatures promote a stronger interaction between Ce atoms from the support and Ni atoms from the metallic phase.

After sample activation, the decrease in temperature revealed a deactivation effect due to active phase re-oxidation. We have determined the point at which both metallic and oxide support are oxidized and what is the overall effect in the product distribution derived from POM reaction. A clear relationship is established between the temperature at which the Ni phase becomes oxidized and the grain or crystallite size. Our results evidence that the larger the Ni crystallite size the slower the oxidation kinetics, thus indicating that re-oxidation effect is limited by oxygen diffusion in the bulk. In addition, evidence of the presence of a spillover mechanism when oxidation of Ce phase takes place was also obtained during POM experiments as oxidation of Ce phase took place immediately after Ni oxidation.

In-situ catalytic tests for partial oxidation of methane revealed a key role from the oxygen of the Ce support in the reaction mechanism and, particularly, a significant modification of the sample activity with grain or crystallite size and specific surface area. Evidence is provided to support that the relationship between oxygen vacancy concentration and catalytic activity is not direct. A higher Ce^{3+}/Ce^{4+} ratio in the NiSDC catalyst support was found to be detrimental to catalytic activity in sample NiSDC900 compared to sample NiSDC1100 that exhibited a moderate concentration of oxygen vacancies. These results highlight the importance of tuning oxygen vacancy concentration in CeO_2-supported Ni catalysts to modulate catalytic activity for methane oxidation.

Acknowledgements

The present work was partially supported by the Brazilian Synchrotron Light Laboratory (LNLS, Brazil, proposals XAFS1 13662, XAFS1 15360 and 20170441, all of them preformed in the D06A-DXAS beamline of the UVX ring), Agencia Nacional de Promoción Científica y Tecnológica (Argentina, PICT 2015 No. 3411, PICT 2016 No. 1921 and PICT 2018 No. 3021) and CAPES-MinCyT bilateral cooperation between Brazil and Argentina. The authors also thank the University of São Paulo for the financial support of NAP-NN (D8-Bruker DaVinci powder diffractometer). M.C.A. Fantini is a CNPq fellow.

References

[1] A. Choya, B. de Rivas, J.R. González-Velasco, J.I. Gutiérrez-Ortiz, R. López-Fonseca, Appl. Catal. A 591 (2020) 117381. https://doi.org/10.1016/j.apcata.2019.117381

[2] F. Matei-Rutkovska, G. Postole, C.G. Rotaru, M. Florea, V.I. Pârvulescu, P. Gelin, Int. J. Hydrogen Energ. 41 (2016) 2512–2525. https://doi.org/10.1016/j.ijhydene.2015.12.097

[3] M. Danielis, L.E. Betancourt, I. Orozco, N.J. Divins, J. Llorca, J.A. Rodríguez, S.D. Senanayake, S. Colussi, A. Trovarelli, Appl. Catal. B 282 (2021) 119567. https://doi.org/10.1016/j.apcatb.2020.119567

[4] T.Y. Liang, P.Y. Low, Y.S. Lin, D.H. Tsai, ACS Appl. Nano Mater. 3 (2020) 9035–9045. https://doi.org/10.1021/acsanm.0c01724

[5] M. Stoian, V. Rogé, L. Lazar, T. Maurer, J.C. Védrine, I.C. Marcu, I. Fechete, Catalysts 11 (2021) 1-42. https://doi.org/10.3390/catal11040427

[6] B. Nematollahi, M. Rezaei, E.N. Lay, Int. J. Hydrog. Ener. 40 (2015) 8539–8547. https://doi.org/10.1016/j.ijhydene.2015.04.127

[7] C. Tang, J. Li, X. Yao, J. Sun, Y. Cao, L. Zhang, F. Gao, Y. Deng, L. Dong, Appl. Catal. A 494 (2015) 77–86. https://doi.org/10.1016/j.apcata.2015.01.037

[8] P. Boizumault-Moriceau, A. Pennequin, B. Grzybowska, Y. Barbaux, Appl. Catal. A 245 (2003) 55–67. https://doi.org/10.1016/S0926-860X(02)00611-7

[9] T. Mishina, N. Fujiwara, S. Tada, A. Takagaki, R. Kikuchi, S.T. Oyama, J. Electrochem. Soc. 167 (2020), 134512. https://doi.org/10.1149/1945-7111/abba65

[10] D.A. Osinkin, Electrochim. Acta, 330 (2020) 135257. https://doi.org/10.1016/j.electacta.2019.135257

[11] P. Li, R. Dong, X. Jiang, S. Zhang, T. Liu, R. Wang, F. Yan, D. Fu, J. Electroanal. Chem. 873 (2020) 114513. https://doi.org/10.1016/j.jelechem.2020.114513

[12] T. Matsui, K. Eguchi, T. Furukawa, T. Okanishi, H. Muroyama, K. Eguchi, J. Electrochem. Soc. 163 (2016) 1146–1150. https://doi.org/10.1149/2.0391610jes

[13] T. Montini, M. Melchionna, M. Monai, P. Fornasiero, Chem. Rev. 116 (2016) 5987–6041. https://doi.org/10.1021/acs.chemrev.5b00603

[14] S. Pengpanich, V. Meeyoo and T. Rirksomboon, Appl. Catal. A. 234 (2002) 221–233. https://doi.org/10.1016/S0926-860X(02)00230-2

[15] P. Li, X. Chen, Y. Li, J.W. Schwank, Catal. Today 327 (2019) 90-115. https://doi.org/10.1016/j.cattod.2018.05.059

[16] J.J. Delgado, E. Del Río, X .Chen, G. Blanco, J.M. Pintado, S. Bernal, J.J. Calvino in Catalysis by ceria and related materials, A. Trovarelli (Ed), Imperial College Press, London, 2013, vol. 12, pp. 47-138.

[17] O.C. Williams, C. Sievers, Appl. Catal. A 614 (2021) 118057. https://doi.org/10.1016/j.apcata.2021.118057

[18] N. Shi, Y. Xie, Y. Yang, S. Xue, X. Li, K. Zhu, D. Huan, R. Peng, C. Xia, Y. Lu, Mater. Renew. Sustain. Energy 9 (2020) 1–18. https://doi.org/10.1007/s40243-020-0166-8

[19] H.A. Shabri, M.H.D. Othman, M.A. Mohamed, T.A Kurniawan, S.M. Jamil, Fuel Process. Technol. 212 (2021) 106626. https://doi.org/10.1016/j.fuproc.2020.106626

[20] L.M. Toscani, M.G. Zimicz, J.R. Casanova, S.A. Larrondo, Int. J. Hydrog. Energ. 39 (2014) 8759-8766. https://doi.org/10.1016/j.ijhydene.2013.12.035

[21] M.G. Zimicz, S.A. Larrondo, R.J. Prado, D.G. Lamas, Int. J. Hydrog. Energ. 37 (2012) 14881–14886. https://doi.org/10.1016/j.ijhydene.2012.01.162

[22] M.G. Zimicz, F.D. Prado, A.L. Soldati, D.G. Lamas, S.A. Larrondo, J. Phys. Chem. C 119 (2015) 19210–19217. https://doi.org/10.1021/acs.jpcc.5b05253

[23] M.G. Zimicz, F.D. Prado, D.G. Lamas, S.A. Larrondo, Appl. Catal. A 542 (2017) 296–305. https://doi.org/10.1016/j.apcata.2017.05.040.

[24] L.M. Toscani, M.G. Zimicz, T.S. Martins, D.G. Lamas, S.A. Larrondo, RSC Adv. 8 (2018) 12190–12203. https://doi.org/10.1039/C8RA01528G.

[25] R. Bacani, L.M. Toscani, T.S. Martins, M.C.A. Fantini, D.G. Lamas, S.A. Larrondo, Ceram. Int. 43 (2017) 7851–7860. https://doi.org/10.1016/j.ceramint.2017.03.101

[26] M.S. Bellora, J. Sacanell, C. Huck-Iriart, A.L. Soldati, S.A. Larrondo, D.G. Lamas, Int. J. Mater. Sci. Appl. 10 (2019) 631–642. https://doi.org/10.4236/msa.2019.1010045

[27] M.G. Zimicz, B.A. Reznik, S.A. Larrondo, Fuel 149 (2015) 95–99. https://doi.org/10.1016/j.fuel.2014.09.024

[28] K. Polychronopoulou, A.F. Zedan, M.S. Katsiotis, M.A. Baker, A.A. AlKhoori, S.Y. AlQaradawi, S.J. Hinder, S. AlHassan, J. Mol. Catal. 428 (2017) 41–55. https://doi.org/10.1016/j.molcata.2016.11.039

[29] P. Venkataswamy, D. Devaiah, K. Kuntaiah, M. Vithal, B. Reddy, Catal. Lett., 147 (2017) 2028–2044. https://doi.org/10.1007/s10562-017-2129-y

[30] R. Tao, J. Xu, H. Zhong, W. Wen, Q. Pan, Y. Liu, J. Chen, Inorg. Chem 58 (2019) 13066-13076. https://doi.org/10.1021/acs.inorgchem.9b01979

[31] R. Raza, B. Zhu, A. Rafique, M.R. Naqvi, P. Lund, Mater. Today Energy 15 (2020) 100373. https://doi.org/10.1016/j.mtener.2019.100373

[32] S. Liu, X. Wu, J. Tang, P. Cui, X. Jiang, C. Chang, W. Liu, Y. Gao, M. Li, D. Weng, Catal. Today 281 (2017) 454-459. https://doi.org/10.1016/j.cattod.2016.05.036

[33] E. Sartoretti, C. Novara, F. Giorgis, M. Piumetti, S. Bensaid, N. Russo, D. Fino, Sci. Rep. 9 (2019) 9-13. https://doi.org/10.1038/s41598-019-39105-5

[34] S. Liu, X. Wu, W. Liu, W. Chen, R. Ran, M. Li, D. Weng, J. Catal. 337 (2016) 188–198. https://doi.org/10.1016/j.jcat.2016.01.019

[35] J. Rodríguez-Carvajal, FULLPROF: a Program for Rietveld Refinement and Pattern Matching Analysis. Satellite Meeting on Powder Diffraction of the XV IUCr Congress, 1990; p 127.

[36] S. Brunauer, P.H. Emmett, E. Teller, J. Am. Chem. Soc. 60 (1938) 309-319. http://dx.doi.org/10.1021/ja01269a023

[37] B. Ravel, M. Newville, J. Synchrotron Radiat. 12 (2005) 537–541. https://doi.org/10.1107/S0909049505012719

[38] P. Fornasiero, G. Balducci, R. Di Monte, J. Kaspar, V. Sergo, G. Gubitosa, A. Ferrero, M. Graziani, J. Catal. 164 (1996) 173−183. https://doi.org/10.1006/jcat.1996.0373

[39] S. Pengpanich, V. Meeyoo, T. Rirksomboon, Catal. Today 93 (2004) 95-105. https://doi.org/10.1016/j.cattod.2004.06.079

[40] H.S. Roh, K.W. Jun, W.S. Dong, J.S. Chang, S.E. Park, Y.I. Joe, J. Mol. Catal. A Chem. 181 (2012) 137-42. https://doi.org/10.1016/S1381-1169(01)00358-2

[43] V. Sharma, P.A. Crozier, R. Sharma, J.B. Adams, Catal. Today 180 (2012) 2–8. https://doi.org/10.1016/j.cattod.2011.09.009

[44] T.J. Huang, C.H. Wang, Catal. Lett. 118 (2007), 103-108. https://doi.org/10.1007/s10562-007-9158-x

[45] Z. Hou, J. Gao, J. Guo, D. Liang, H. Lou, X. Zheng, J. Catal. 250 (2007) 331–341.

https://doi.org/10.1016/j.jcat.2007.06.023

Graphical abstract

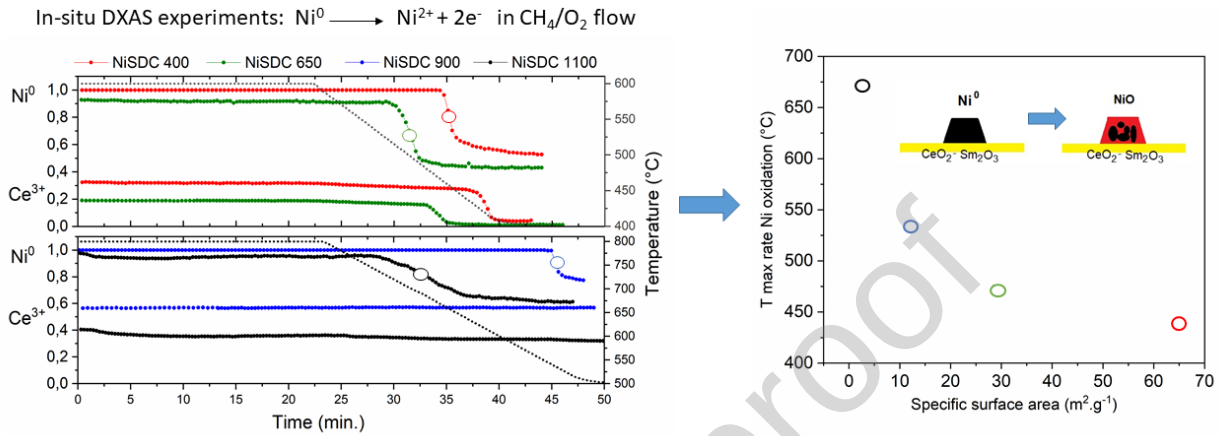

CRediT authorship contribution statement

Lucía M. Toscani: Investigation, Formal analysis, Writing - Original Draft preparation, **Marina Bellora.**: Investigation, Formal analysis, Writing - Review & Editing , **Cristián Huck-Iriart**: Investigation, Formal analysis, Software, Visualization, Writing - Review & Editing, **Analía Soldati**: Investigation, Formal analysis, Writing - Review & Editing, **Joaquín Sacanell**: Investigation, Supervision, Writing - Review & Editing , **Tereza Martíns**: Investigation, Supervision, Writing - Review & Editing , **Aldo Craievich**: Investigation, Supervision, Writing - Review & Editing, **Márcia C. A. Fantini**: Investigation, Supervision, Writing - Review & Editing, **Susana A. Larrondo**: Investigation, Supervision, Writing - Review & Editing, **Diego Lamas*:*** Conceptualization, Methodology, Writing - Original Draft preparation

Declaration of Competing Interests

☒ The authors declare that they have no known competing financial interests or personal relationships that could have appeared to influence the work reported in this paper.

☐The authors declare the following financial interests/personal relationships which may be considered as potential competing interests:

Highlights

- Redox behavior significantly depends on grain size and surface area.
- Sample deactivation occurs due to re-oxidation of metallic phase.
- Temperature of maximum rate of Ni oxidation is directly correlated to grain size.
- Ce reduction is enhanced by H_2 spillover mechanism over metallic Ni particle
- An excessive concentration of oxygen vacancies is detrimental to catalytic activity.